Epithelial and Mesenchymal Tumor Compartments Exhibit *In Vivo* Complementary Patterns of Vascular Perfusion and Glucose Metabolism[1]

Mirco Galiè*, Paolo Farace*, Cristina Nanni[†], Antonello Spinelli[‡], Elena Nicolato*, Federico Boschi*, Paolo Magnani*, Silvia Trespidi[†], Valentina Ambrosini[†], Stefano Fanti[†], Flavia Merigo*, Francesco Osculati*, Pasquina Marzola* and Andrea Sbarbati*

*Dipartimento Scienze Morfologico-Biomediche, sez. Anatomia ed Istologia, Università di Verona, Verona, Italy; [†]UO Medicina Nucleare, Azienda Ospedaliero-Universitaria di Bologna Policlinico S. Orsola-Malpighi, Bologna, Italy; [‡]Servizio di Fisica Sanitaria, Azienda Ospedaliero-Universitaria di Bologna Policlinico S. Orsola-Malpighi, Bologna, Italy

Abstract

Glucose transport and consumption are increased in tumors, and this is considered a diagnostic index of malignancy. However, there is recent evidence that carcinoma-associated stromal cells are capable of aerobic metabolism with low glucose consumption, at least partly because of their efficient vascular supply. In the present study, using dynamic contrast-enhanced magnetic resonance imaging and [F-18]fluorodeoxyglucose (FDG) positron emission tomography (PET), we mapped *in vivo* the vascular supply and glucose metabolism in syngeneic experimental models of carcinoma and mesenchymal tumor. We found that in both tumor histotypes, regions with high vascular perfusion exhibited a significantly lower FDG uptake. This reciprocity was more conspicuous in carcinomas than in mesenchymal tumors, and regions with a high-vascular/low-FDG uptake pattern roughly overlapped with a stromal capsule and intratumoral large connectival septa. Accordingly, mesenchymal tumors exhibited a higher vascular perfusion and a lower FDG uptake than carcinomas. Thus, we provide *in vivo* evidence of vascular/ metabolic reciprocity between epithelial and mesenchymal histotypes in tumors, suggesting a new intriguing aspect of epithelial–stromal interaction. Our results suggests that FDG-PET–based clinical analysis can underestimate the malignity or tumor extension of carcinomas exhibiting any trait of "mesenchymalization" such as desmoplasia or epithelial–mesenchymal transition.

Neoplasia (2007) **9,** 900–908

Keywords: Metabolism, vasculature, tumor, PET, MRI.

Introduction

Glucose transport and consumption are increased in tumors, and this is considered a diagnostic index of malignancy [1–4]. Based on this assumption, [F-18]fluorodeoxyglucose (FDG) positron emission tomography (PET) is being used in clinical practice for tumor diagnosis and volume delineation before therapeutic treatment [5–9]. However, recent work has demonstrated differential glucose absorption between epithelial and stromal compartments within carcinomas, revealing the synergistic complementarities of their metabolism [10]. Cancer cells have an inherent tendency for anaerobic glycolysis [11,12], which is massively enhanced by a lack of adequate blood supply [13–16] and leads to abnormal glucose consumption and lactate extrusion. Conversely, tumor-associated stromal cells are capable of aerobic metabolism with low glucose consumption, and it has been proposed that they could clear and recycle the lactate produced by the anaerobic metabolism of cancer cells [10]. This is a further intriguing aspect of epithelial–stromal interaction and is consistent with the high angiogenic potential of tumor-associated reactive stromal cells [17,18], which provide mesenchymal compartments with adequate blood supply [19]. Thus, we hypothesized that the combination of FDG-PET and dynamic contrast-enhanced magnetic resonance imaging (DCE-MRI) can discriminate *in vivo* the epithelial and stromal compartments in carcinomas.

Furthermore, the anatomic distinction between epithelial and mesenchymal compartments in carcinomas, particularly of the breast, is an aspect of tumor biology that is currently undergoing revision. Not uncommonly, carcinomas reveal colocalization of mesenchymal and epithelial markers or exhibit abnormally developed stroma (desmoplasia) [20]; in some cases, they can even transdifferentiate into carcinosarcomas or monophasic sarcomas, usually proving malignant in either case [21,22]. The "mesenchymalization" of carcinomas has recently been described also in transgenic murine models of HER-2/neu carcinomas [23,24] and represents a possible mode of tumor recurrence [25]. This experimental evidence

prompts speculation that the capacity to generate mesenchymal tumors is inherent in carcinomas and that they can arise autonomously if the epithelium is attacked, for instance after therapeutic treatment [26]. In line with this evidence, we have recently established a HER-2/neu−negative mesenchymal cell lineage, called A17, from a HER-2/neu transgenic mammary tumor, a subcutaneous injection (into syngeneic mice) of which led to the development of mesenchymal tumors [27]. If the extent of glucose absorption in carcinomas results from the relative contribution of the epithelial and stromal compartments, it is reasonable to suppose that it is affected by any form of mesenchymalization and, in particular, by complete transdifferentiation toward a sarcomatoid phenotype.

To investigate these hypothesis, we used FDG-PET [1] and DCE-MRI [28] to comparatively map, *in vivo*, the glucose consumption and vascular perfusion of previously described [27] syngeneic murine models of spontaneous and transplanted (BB1) carcinoma and carcinoma-derived sarcoma (A17).

Materials and Methods

Tumor Models

The spontaneous and transplanted tumors used in this study have already been described. Briefly, spontaneous tumors were mammary carcinomas that arose in FVB mice (line 233) that were transgenic for the activated isoform of rat HER-2/neu (*NeuNT*) oncogene (FVB/neuT233) and were purchased from Charles River Laboratories (Calco, Italy). The A17 and BB1 cell lines were established from spontaneous HER-2/neu transgenic tumors. Subcutaneous injection of BB1 cells into syngeneic mice led to the development of mammary carcinomas that were morphologically and immunohistochemically analogous to spontaneous tumors (i.e., strongly positive for HER-2/neu, cytokeratins 8 and 18, and E-cadherin). Subcutaneous injection of A17 cells into syngeneic mice led to mesenchymal tumors that were negative for the expression of HER-2/neu, cytokeratins 8 and 18, and E-cadherin, but positive for the expression of mesenchymal markers such as vimentin [27]. Carcinoma-derived mesenchymal tumors were induced by subcutaneous injection of A17 cells. In detail, BB1 and A17 tumors were obtained by subcutaneous injection of 5×10^5 cells into the back of 5- to 7-week-old female FVB/neuT233 mice. Tumor growth was monitored, and tumor size was measured weekly using calipers. The animals underwent DCE-MRI and PET when the longest diameter of their tumors had reached 10 to 15 mm. The investigation complied with national legislation on the care and use of laboratory animals.

Image Acquisition
DCE-MRI. Animals were examined using MRI with Gd-DTPA-albumin as a contrast agent, and again 48 hours later using Gd-DTPA (Magnevist; Schering, Berlin, Germany). The mice were anesthetized by inhalation of a mixture of air and O_2 containing 0.5% to 1% isoflurane and were placed in prone position inside a 3.5-cm-i.d. transmitter−receiver birdcage coil. Images were acquired using a Biospec tomo-

graph (Bruker, Karlsruhe, Germany) equipped with a 4.7-T 33-cm bore horizontal magnet (Oxford Ltd., Oxford, UK). Coronal spin-echo and transverse multislice fast spin T_2-weighted images ($T_{E\ eff}$ = 70 milliseconds) were acquired for tumor localization and good visualization of extratumoral tissues. Precontrast T_1 values of tumor tissues were measured using the IR-SnapShot Flash technique (Bruker, Karlsruhe, Germany) in a limited number of animals (n = 3) because the average T_1 value did not change significantly across the tumor tissues.

A dynamic series of transverse spoiled gradient-echo 3D images was acquired with the following parameters: repetition time/echo time = 50/3.5 milliseconds; flip angle = 90°; matrix size = 256 × 128 × 16; field of view = 6 × 3 × 2.4 cm^3 (corresponding to 0.234 × 0.234 mm^2 in-plane resolution and 1.5 mm slice thickness); number of acquisitions = 1. The acquisition time for a single 3D image was 102 seconds; dynamic scans of 24 images were acquired at 3-second intervals (total acquisition time, ~ 42 minutes). The contrast agents Gd-DTPA-albumin and Magnevist at 90 and 500 μmol/kg, respectively, were injected in bolus during the interval between the first scan and the second scan. A phantom containing 1 mM Gd-DTPA in saline was inserted in the field of view and used as an external reference standard.

To calculate transendothelial permeability (Kps), the plasma kinetics of contrast media was determined in a separate experiment, as previously described [29], and carried out in a total of six normal animals (three animals for each contrast agent).

PET image acquisition and reconstruction. FDG-PET scanning was carried out as follows: animals were anesthetized with gas anesthesia (3−5% sevoflurane and 1 l/min oxygen) and injected with 30 MBq of FDG, at a volume of 0.1 ml, through the tail vein using an insulin syringe. The animals were subsequently allowed to wake up for the uptake time (60 minutes) and were free to move. Residual dose was measured to verify the dose effectively injected. Finally, the same anesthetizing procedure was repeated to perform the scan. Each anesthetized animal was placed on a scanner bed in prone position. Images were acquired with a Small Animal PET tomograph (GE eXplore Vista DR; GE Healthcare, Fairfield, CT) [30] for a total acquisition time of 20 minutes. Given the size of the animals, no corrections for attenuation or scatter were performed. As the axial field of view was 4 cm, one bed position was sufficient to cover most of the mouse body. Once the scan was finished, the gas anesthesia was interrupted and the animal was placed in a recovery box with warm temperature until complete recovery.

Images were reconstructed with iterative reconstruction on OSEM 2D (Siemens, Munich, Germany) using 2 iterations and 32 subsets after Fourier rebinning. The voxel dimensions of the reconstructed images were 0.38 × 0.38 × 0.77 mm^3. The scan was considered positive if areas of increased FDG uptake were present in sites consistent with the site of injection.

Computed tomography image acquisition and computed tomography PET registration. Computed tomography (CT) scanning was performed using a dedicated small animal CT

scanner (GE eXplore Locus), and mice were anesthetized analogously to PET acquisitions. CT images were reconstructed using filtered backprojection, and the resulting voxel dimensions were $0.18 \times 0.18 \times 0.18$ mm^3. To perform PET and CT image registration, at least four molecular sieves soaked with FDG were placed around the animal as reference points, and rigid body transformation was calculated to fuse PET and CT images. Image registration and fusion were obtained using a dedicated software (MicroView; GE Healthcare).

Image Analysis

Image selection.   To comparatively map vascular perfusion and FDG uptake, we selected roughly corresponding FDG-PET and MRI sections using the procedure described in Figure 1. The MRI images shown were obtained by pixel-by-pixel subtraction of the third postcontrast image from the precontrast image. Gd-DTPA (a low-molecular-weight contrast agent) was chosen for this MRI-PET comparative analysis to approximate the distribution of small molecules such as FDG. We examined early enhancement (third of 30 acquisitions) on the assumption that, in later phases, the contrast agent reaches nonvascularized regions by convection [31], thus compromising a clear discrimination between regions with high and low vessel densities.

FDG-PET of high and low vascular regions.   High-vascularization and low-vascularization regions of interest (ROI) were chosen manually on MRI subtraction images by picking regions that exhibited high and low enhancement, respectively (Figure 1). The signal intensities of ROI were calculated and normalized with respect to the signal intensity of the external reference standard to obtain comparable values of signal enhancement. The same regions were identified in roughly corresponding FDG-PET sections. The FDG uptake of these regions was calculated and normalized with respect to the mean value of the liver, using tumor-to-nontumor ratio (T/N) [32].

Comparative analysis of the vascular perfusion of the epithelial and stromal compartments.   To find vascular differences between tumor epithelial and stromal compartments, MRI signal enhancement of manually drawn ROI covering the pericapsular region or tumor core was measured on images obtained by subtracting the most enhanced postcontrast image (3rd for Gd-DTPA MRI or 24th for Gd-DTPA-albumin MRI) from the precontrast image of the same section. Ratios of values from the pericapsular region and tumor core were calculated accordingly. Three contiguous sections per tumor, including the one previously selected, were analyzed.

Comparative analysis of FDG uptake and vascular perfusion in carcinoma and mesenchymal tumors.   An ROI drawn to encompass the whole tumor made it possible to obtain the dynamics of signal enhancement and concentration–time curves for each sample. Vascular perfusion was evaluated by the mean concentration value of Gd-DTPA obtained during dynamic scanning. Following previously published protocols [33], from the time dependence of the contrast agent concentration, we evaluated the average Kps of the tumors for both Gd-DTPA and Gd-DTPA-albumin [29].

Semiquantitative analysis of FDG uptake was performed by drawing the volume of interest (VOI) to encompass the whole tumor and by drawing a background VOI to obtain T/N values. For background on sections covering the liver, a VOI was drawn inside the parenchyma in each animal scan. The mean and maximal voxel values inside each VOI were evaluated accordingly.
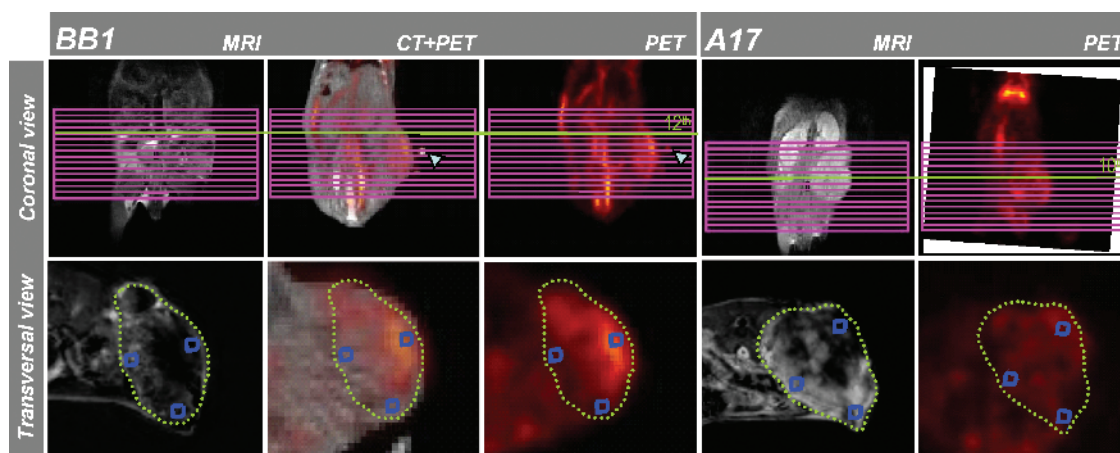

Figure 1. *Selection and matching of coarsely corresponding Gd-DTPA-MRI and FDG-PET tumor sections. Each tumor underwent MRI and FDG-PET analysis. For BB1 tumors, CT images were also acquired and coregistered with FDG-PET using at least four spatial markers as reference (cyan arrowheads). One MRI transverse slice per tumor was chosen. The MRI geometric multislice grid was positioned on the coronal view of PET (or CT-PET–registered) acquisitions and used as spatial reference to identify roughly corresponding transverse tumor sections. MRI images were obtained on pixel-by-pixel subtraction of the third postcontrast and the last precontrast dynamic image (see Materials and Methods). For each tumor, two to four ROI (blue frames) were placed on high- and low-enhanced regions of MRI images, and corresponding ROI were identified in CT-PET and/or PET sections. The values of MRI enhancement were normalized with respect to the signal intensity of the reference standard. The values of FDG uptake were normalized with respect to the mean value of the liver.*

Statistical Analysis

The statistical significance of the differences in MRI signal enhancement between the tumor periphery and the tumor core for each tumor was evaluated using paired *t*-test.

The statistical significance of the different parameters was evaluated using two-tailed unequal-variance *t*-test. $P < .05$ was considered statistically significant.

Postmortem Analysis

Histologic analysis. Tumors excised from sacrificed mice were fixed in zinc fixative, dehydrated, cut in half transversally, and embedded in paraffin wax. The halves were blocked and processed separately, with the cut edge ultimately facing the microtome surface. Two consecutive sections were taken from the face of each block, and then additional sections were taken at 100-μm intervals as far as roughly 1 mm into each block. Sections (5 μm) were cut on a rotary microtome and placed on polylysine-coated slides for morphologic analysis.

The sections obtained were in planes corresponding approximately to those used in MRI and PET evaluations.

Vessel immunostaining. Half of each of the tumor samples was fixed in paraformaldeyde (4%) and frozen. Endothelial cells of three sections per tumor were immunostained with anti-CD31–specific antibody (BD PharMingen, San Diego, CA) to visualize their vascular network. Specimens were examined with a Zeiss LSM 510 confocal microscope (Zeiss, Oberkachen, Germany) equipped with argon (488 nm) and helium/neon (543 nm) excitation beams.

Results

Highly Vascularized Regions in Tumors Exhibit Low FDG Uptake

Using the procedure described in Figure 1, we matched roughly corresponding Gd-DTPA-MRI and FDG-PET tumor sections of four BB1 carcinomas and four A17 mesenchymal tumors.

The signal enhancement of highly vascularized regions was 0.198 ± 0.07 for BB1 tumors and 0.65 ± 0.3 for A17 tumors. The signal enhancement of poorly vascularized regions was 0.062 ± 0.035 for BB1 tumors and 0.19 ± 0.13 for A17 tumors ($P < .01$ for both tumor histotypes).

Considering all the eight tumors together, we found that highly vascularized regions exhibited significantly lower FDG uptake than regions with low vascularization (T/N: 1.37 ± 0.39 *vs* 1.99 ± 0.55, $P < .005$) (Figure 2). Considering the single histotypes separately, BB1 tumors showed a greater difference between FDG uptake in high-MRI–enhanced and low-MRI–enhanced regions (T/N: 1.35 ± 0.48 *vs* 2.1 ± 0.60, $P < .05$) than A17 tumors (T/N: 1.38 ± 0.40 *vs* 1.80 ± 0.45, $P = .13$), suggesting a greater heterogeneity of MRI and FDG maps in carcinomas than in the mesenchymal tumor histotype.
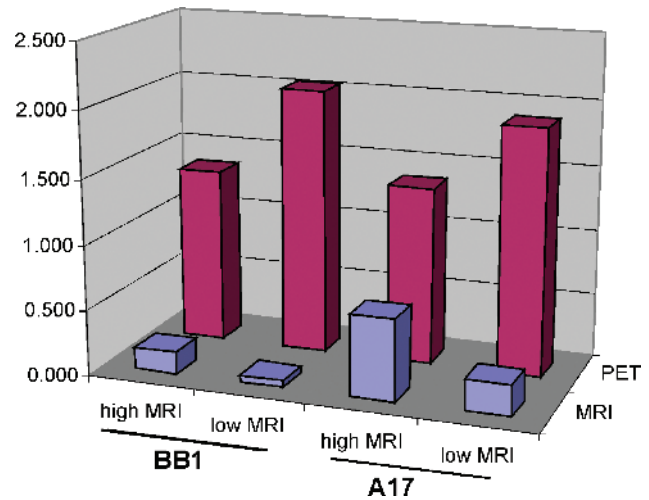

Figure 2. *Comparative analysis of MRI enhancement in carcinomas (BB1) and mesenchymal tumors (A17). In both BB1 and A17 tumors, FDG uptake proved higher in high-MRI– than in low-MRI–enhanced regions.*

Differential Spatial Distribution of Gd-DTPA and FDG Uptake in Pericapsular Region and Intratumoral Connectival Septa

The vascular supply in carcinomas is provided by tumor stroma. We were therefore interested in assessing whether regions with a high-vascular/low-FDG uptake pattern corresponded to the stromal compartment in carcinomas. MRI analysis was performed on five tumors. We found that the enhancement of MRI signal intensity was significantly higher at the tumor periphery than at the tumor core, with both Gd-DTPA (1.25 ± 0.24-fold, $P < .01$) and Gd-DTPA-albumin (2.08 ± 1.67-fold, $P < .01$) partly overlapping with the highly vascularized tumor capsule [34] along with a moderately vascularized subcapsular layer (Figure 3, *A–D*). Inside the tumor parenchyma, contrast enhancement roughly matched large intratumoral stromal septa (Figure 3, *B* and *D*). In contrast, FDG uptake was observed inside the tumor parenchyma, which was mainly composed of epithelial cells, except in correspondence with necrotic areas (Figure 3, *C* and *E*), and showed discontinuities in correspondence with large intratumoral connectival septa (Figure 3, *D* and *F*).

With the aim of investigating whether vascular differences between tumor rim and tumor core are typical of carcinomas or are independent of tumor histotype, we performed the same analysis on A17 tumors, which were composed of the homogeneous parenchyma of mesenchymal cells and did not show a distinguishable stromal capsule, except where tumor parenchyma invaded the cutis (Figure 3, *G–I*). MRI analysis was performed on five tumors. Although the signal enhancement induced by MRI tracers was higher at the tumor periphery than at the core with both Gd-DTPA (1.20 ± 0.35–fold) and Gd-DTPA-albumin (1.08 ± 0.42–fold), the differences were not statistically significant ($P > .05$).

Differential Spatial Distribution of Gd-DTPA and FDG Uptake in Spontaneous Tumors

To further exploit the reciprocal pattern of vascular perfusion and glucose metabolism, we performed PET and
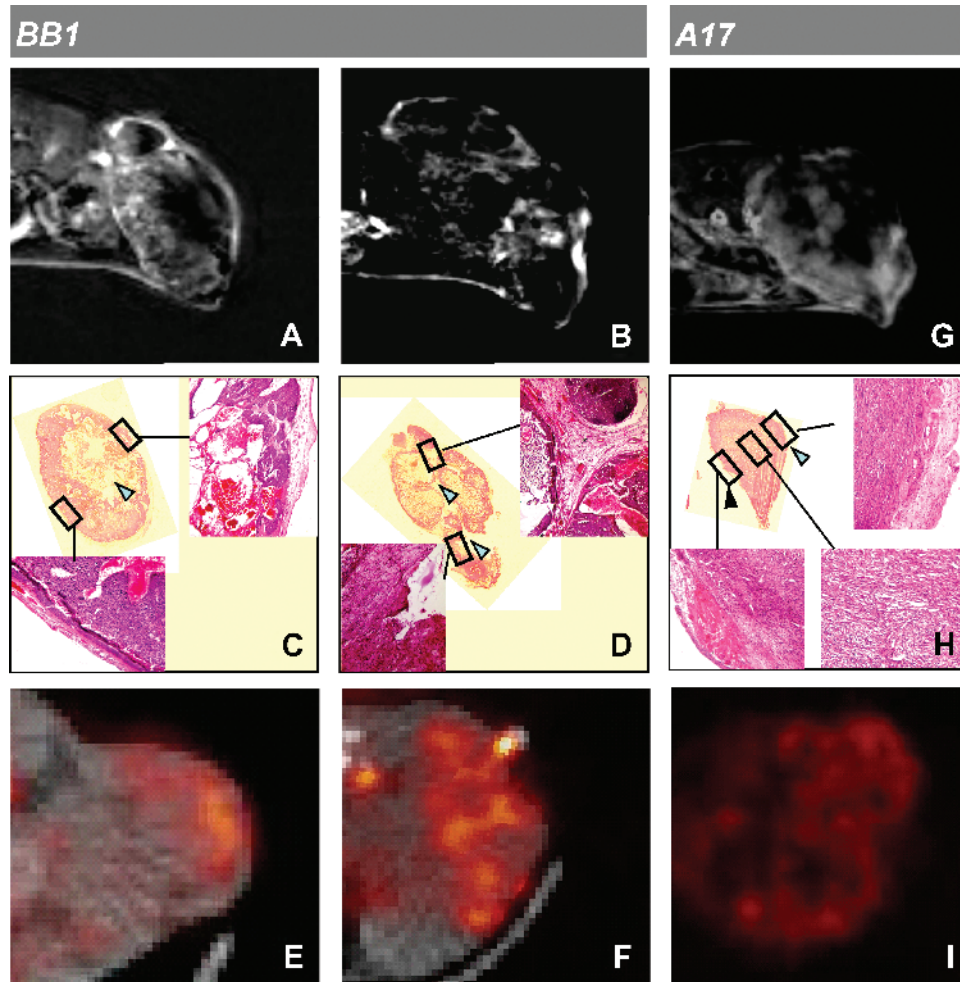
Figure 3. *Mapping of perfusion and metabolic patterns in transplanted tumors. On BB1 tumors, third postcontrast minus precontrast images after Gd-DTPA injection showed enhancement at the tumor periphery, typical of carcinomas (A), or, less frequently, in restricted regions of the intratumoral parenchyma (B). On histologic analysis, the peripheral areas of enhancement matched peritumoral capsule and an epithelial subcapsular layer. MRI enhancement showed discontinuities in correspondence with necrotic areas (C) and, inside the tumor parenchyma, roughly matched large intratumoral stromal septa (D; arrowhead). The surrounding epithelial parenchyma showed progressively lower cellular density as distance from intratumoral connectical septa increased. FDG uptake showed a complementary pattern to Gd-DTPA distribution (E and F). Corresponding CT images were overlapped on PET images to allow tumor delineation. On A17 tumors, third postcontrast minus precontrast images after Gd-DTPA injection showed evident—although inhomogeneous—intratumoral enhancement (G). On histologic analysis (H), tumor parenchyma proved homogeneous from the periphery to the core with only a small focus of necrosis (black arrowhead) and did not exhibit a stromal capsule except at the external side, where tumor invaded the skin (cyan arrowheads). FDG uptake exhibited an inhomogeneous pattern (I) that is roughly complementary to MRI tracer enhancement.*

Gd-DTPA analysis on carcinomas that spontaneously arose in four HER-2 transgenic mice.

We also applied a more precise procedure to select the corresponding PET and MRI sections: After PET scans, the molecular sieves placed around the animals as reference points were replaced by pieces of blotting paper embedded with vegetable oil detectable on MR images. By rigid transformation, a better alignment of MRI and PET sections was obtained, despite unavoidable changes in animal position due to the different animal couch. In this tumor model, large necrotic areas, which did not appreciably enhance on both PET and MRI, were revealed. Viable tumor tissues surrounding large unenhancing areas evidenced a complementary amount of FDG and Gd-DTPA uptake, with regions of higher and lower FDG consumption characterized, respectively, by lower and higher signal intensities on the early phase of contrast MRI enhancement (Figure 4).

Carcinoma-Derived Mesenchymal Tumors (A17) Exhibit Higher Vascular Perfusion But Lower FDG Uptake Than Syngeneic Carcinomas (BB1)

We observed that a complementary pattern of vascular perfusion and FDG uptake comparing BB1 carcinomas and A17 mesenchymal tumors was reproduced.

MRI enhancement in A17 tumors, which was measured by taking the entire tumor section into account, was significantly higher than that in BB1 tumors (Table 1). In contrast, FDG uptake by A17 tumors proved significantly lower than that by BB1 tumors, taking both mean and maximal values into consideration (Table 1).

Several authors have investigated the correlations between vascular parameters and FDG uptake in human tumors, with contrasting results: DCE-MRI–assessed Kps has been reported to be directly or inversely correlated with glucose metabolism [35,36]. In this study, we evaluated the
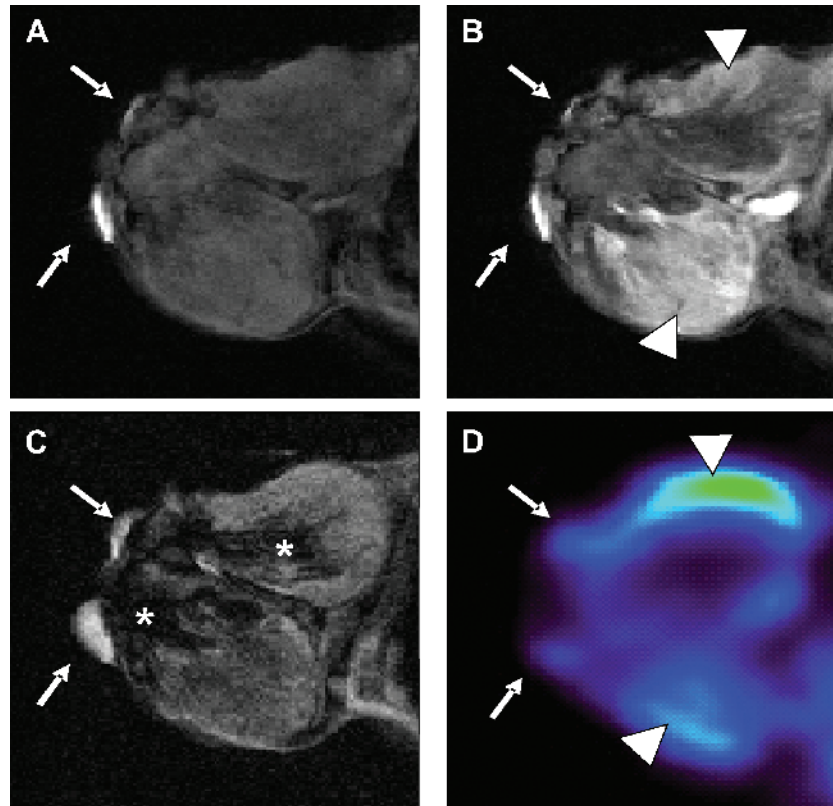
Figure 4. *Mapping of perfusion and metabolic pattern on spontaneous carcinomas. Precontrast (A), early postcontrast (B), T_2-weighted (C), and FDG-PET (D) corresponding sections of a spontaneous breast carcinoma. External reference points (white arrows) were used to obtain better alignment between MRI and PET scan. A large hemorrhagic necrotic area was appreciable in a T_2 image (asterisks), which did not enhance on postcontrast MRI and did not take up FDG. Viable tumor tissues evidenced areas of higher and lower FDG consumption (arrowhead) revealing, respectively, lower and higher Gd-DTPA enhancement.*

Kps of A17 and BB1 tumors using DCE-MRI with both extravascular (Gd-DTPA) and intravascular (Gd-DTPA-albumin) contrast agents, and we investigated its correlation with FDG uptake. In accordance with previous observations [27,37],

A17 tumors exhibited significantly ($P < .05$) higher Kps than BB1 tumors (Table 1) with Gd-DTPA-albumin. This result was confirmed by DCE-MRI with GD-DTPA, although statistical significance was weak ($P = .07$). It was consistent with

Table 1. Quantitative Analysis of FDG-PET and DCE-MRI Examinations.

	FDG-PET		DCE-MRI		
	T/N		Mean Concentration (mM)	Kps [(ml/min) per cm^3]	
	Mean	Maximal	Gd-DTPA	Gd-DTPA	Gd-DTPA Albumin
BB1	1.94	2.63	0.59	0.021	0
	2.27	2.78	NA	NA	NA
	2.32	3.01	0.53	0.0145	0.0005
	2.46	3.50	0.60	0.017	0
	2.08	2.77	0.47	0.017	0.0005
	2.19	2.93	NA	NA	NA
Mean ± SD	2.20 ± 0.20	2.97 ± 0.33	0.55 ± 0.06	0.017 ± 0.002	0.00025 ± 0.0003
A17	1.35	1.85	NA	NA	NA
	1.91	2.77	0.97	0.033	0.0018
	1.73	2.25	0.71	0.028	0.0015
	1.54	2.37	0.91	0.047	0.0007
	1.93	2.54	0.60	0.017	0.0017
	1.64	2.10	NA	NA	0.0009
Mean ± SD	1.69 ± 0.22	2.31 ± 0.32	0.80 ± 0.17	0.03 ± 0.01	0.0013 ± 0.0005
Statistical significance (P)	.003	.009	.003	.07	.006

For FDG-PET analysis, we report the mean and maximal T/N values of the VOI, which encompassed the whole section of the tumors. For DCE-MRI, the mean concentration values of Gd-DTPA over the acquisition time are reported, and Kps was obtained from the two-compartment kinetic analysis of both Gd-DTPA and Gd-DTPA-albumin enhancement curves. Statistical significance refers to the comparison between the BB1 and A17 tumor groups.

histologic features of A17 vessels, which frequently appeared smaller in size but had a higher surface/volume ratio than BB1 vessels (Figure 5).

Intragroup analysis (i.e., only of the A17 group, or of the BB1 group) showed no statistically significant correlation between FDG uptake and perfusion parameters.

Both Carcinomas and Mesenchymal Tumors Exhibit Enhanced Metabolism with Respect to Nontumor Tissues

FDG-PET is being used in clinical practice as a tool for tumor diagnosis, on the assumption that tumors exhibit an inherently enhanced glucose metabolism with respect to surrounding normal tissues. Our results confirmed this assumption, as FDG uptake values in carcinomas and mesenchymal tumors proved higher than the mean values of nontumor reference tissues (liver), whether the entire tumor section (Table 1; BB1, T/N = 1.94−2.46; A17, T/N = 1.35−1.93), or the most highly FDG-enhanced regions (BB1, T/N = 1.18−3.07; A17, T/N = 1.41−2.53), or the regions with the lowest FDG enhancement (BB1, T/N = 0.83−1.77; average = 1.35 ± 0.41; A17, T/N = 0.85−1.94; average = 1.38 ± 0.40) were taken into account.

Discussion

Our results involve pressing questions in tumor biology and clinical oncology. We demonstrated a complementary spatial pattern of vascular perfusion and glucose metabolism in tumors. After we had finished this study, an *in vivo* mapping study by Raman et al. [38] demonstrated a complementary pattern of vascular volume and hypoxia in a model of prostate cancer. Their data are consistent with ours, as it is well known that hypoxia enhances glucose uptake through the opening of GLUT-1 transporters [39].

Vascular/Metabolic Reciprocity within Carcinomas

We showed that this reciprocity is greater in carcinomas than in mesenchymal tumors, and that it was associated with the spatial distribution of the epithelial and stromal compartments. In transplanted carcinomas (BB1), vascular supply proved higher at the tumor periphery, as shown for human cancers [40], partly corresponding to the stromal capsule, than inside the tumor. In contrast, FDG uptake proved higher in the middle of non-necrotic tumor parenchyma, where epithelial tissue was prevalent. Where large intratumoral connectival septa were observed, the pattern of DCE-MRI and FDG uptake was inverted. Thus, we provide *in vivo* evidence of an intriguing aspect of epithelial−stromal interaction in carcinomas showing vascular and metabolic reciprocity between these two tumor compartments. This complementary pattern can be explained by recent evidence of synergistic metabolic interaction between epithelial and mesenchymal cell populations. Tumor blood vessels are distributed mainly within the stromal compartment, and the role of stromal cells in promoting their generation and organization has been extensively examined. As tumors grow, epithelial cells are found progressively farther from blood vessels as the distance from intratumoral connectival septa increases, and scarcity of oxygen contributes to the switching of their metabolism toward anaerobic processes, which ultimately produce lactate. Abundant oxygen supply to tumor-associated stromal cells allows them not only to produce
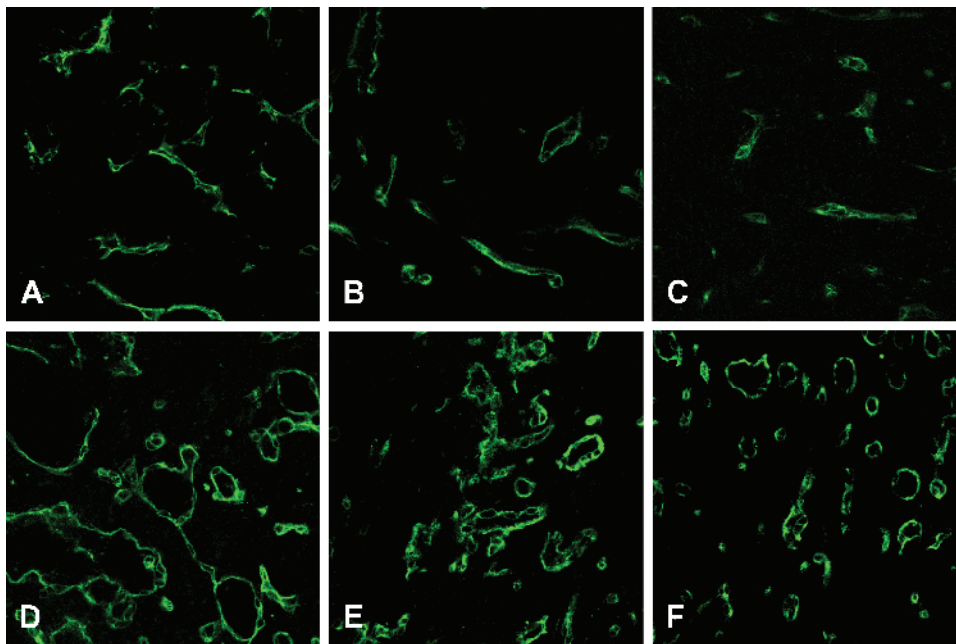

Figure 5. *Histologic analysis of tumor vessels. On CD31 immunostaining, vessels of A17 tumors were more numerous and uniformly distributed inside the tumor parenchyma, but were smaller in size (A−C) than vessels of BB1 (D−F), which were mainly found at the tumor periphery. Because BB1 vessels are only restricted to occasionally stromal regions of the tumor, the reported images are representative only of the highly vascularized area (stromal septa). The higher surface/ volume ratio appeared consistent with the significantly higher Kps of A17 tumors compared with BB1 tumors (Table 1).*

energy aerobically but also to recycle the lactate released by cancer cells. Thus, the epithelial and stromal populations of growing tumors can be viewed as two parts of a functional domain with genuine metabolic cooperation between anaerobic and aerobic compartments [10,41].

Vascular/Metabolic Reciprocity between Epithelial and Mesenchymal Histotypes

The complementarities observed between epithelial and mesenchymal compartments of the same carcinomas were again found between epithelial and mesenchymal tumor models raised by the subcutaneous injection of cell lines derived from the same mammary carcinoma. A17 tumors exhibited a higher mean MRI enhancement and a lower mean FDG uptake than BB1 carcinomas. The shift of carcinomas toward a mesenchymal phenotype is a matter of concern in clinical oncology, as it represents a poor prognostic factor [42]. In addition, the scarcity of oxygen, which is inherent in carcinomas, can provide a decisive contribution to the generation of tumor-promoting or tumorigenic mesenchymal populations. Stromal cells at the invasive tumor front are directly activated by anoxia, as occurs physiologically in wound-healing processes [43]. Normal fibroblasts responding to anoxia exhibit features of malignant phenotype because their proliferation increases and triggers proangiogenic, antiapoptotic, locomotor, and invasive programs [41,44–47]. In any case, recent studies on experimental models of HER-2/neu tumors demonstrated that the possibility of developing into mesenchymal tumors is inherent in carcinomas. Hill et al. [23] showed that the neoplastic epithelial compartment induces aberrant evolution of genetically altered stromal mesenchyme. Moody et al. [25] found that mesenchymal tumors can spontaneously arise as recurrences after the regression of primary tumors in an inducible HER-2/neu model of carcinoma [48]. Knutson et al. [24] and Moody et al. [25] showed that anti−HER-2/neu−specific immune response can select neu-negative mammary tumors with mesenchymal phenotype. This evidence greatly enhances the clinical significance of experimental models of carcinoma-derived mesenchymal tumorigenic cells.

Several authors have investigated the correlations between vascular parameters and FDG uptake in human tumors, providing controversial results [35,36]. In accordance with previous observations [27,37], here we found that A17 tumors exhibited significantly higher Kps than BB1 tumors. However, intragroup correlation between FDG uptake and MRI-measured Kps in our experimental model did not reach statistical significance. This probably reflects the fact that the relationship between glucose metabolism and blood supply is affected by a number of (morphologic or biochemical) factors [49,50].

Potential Clinical Implications

Given that *in vivo* assessment of glucose metabolism by FDG-PET is being used in clinical practice for tumor diagnosis/grading and therapy monitoring, our results highlight the risk of underestimating the malignity of carcinomas that are highly vascularized and/or exhibit any traits of mesen-

chymalization, such as desmoplasia [51] or epithelial−mesenchymal transition [52]. In particular, lower glucose consumption of the stromal compartment could make FDG-based pretreatment tumor delineation difficult. The exact definition of tumor extension has a profound impact on tumor local control, which justifies the enormous expenditure involved in multiple noninvasive imagings performed in clinical practice. In this respect, FDG distribution is proposed not only for lymph node staging but also to delineate gross tumor volume for planning radiotherapy treatments [6,7], but only occasionally is delineation based on FDG-PET compared with pathological examination [8], and studies with similar design are awaited [9]. Our findings alert to the risk that only part of the tumor could be treated in some cases because it appears that such approach could limit therapy to the lowest vascularized regions, adding biologic consideration to the opinion that PET-directed tumor volume contouring is not ready for clinical practice without further technological improvements in imaging specificity/sensitivity [53].

References

[1] Mamede M, Higashi T, Kitaichi M, Ishizu K, Ishimori T, Nakamoto Y, Yanagihara K, Li M, Tanaka F, Wada H, et al. (2005). [18F]FDG uptake and PCNA, Glut-1, and Hexokinase-II expressions in cancers and inflammatory lesions of the lung. *Neoplasia* **7**, 369–379.

[2] Kurokawa T, Yoshida Y, Kawahara K, Tsuchida T, Okazawa H, Fujibayashi Y, Yonekura Y, and Kotsuji F (2004). Expression of GLUT-1 glucose transfer, cellular proliferation activity and grade of tumor correlate with [F-18]-fluorodeoxyglucose uptake by positron emission tomography in epithelial tumors of the ovary. *Int J Cancer* **109**, 926–932.

[3] Miller TR, Pinkus E, Dehdashti F, and Grigsby PW (2003). Improved prognostic value of 18F-FDG PET using a simple visual analysis of tumor characteristics in patients with cervical cancer. *J Nucl Med* **44**, 192–197.

[4] Higashi T, Tamaki N, Torizuka T, Nakamoto Y, Sakahara H, Kimura T, Honda T, Inokuma T, Katsushima S, Ohshio G, et al. (1998). FDG uptake, GLUT-1 glucose transporter and cellularity in human pancreatic tumors. *J Nucl Med* **39**, 1727–1735.

[5] Lardinois D, Weder W, Hany TF, Kamel EM, Korom S, Seifert B, von Schulthess GK, and Steinert HC (2003). Staging of non−small-cell lung cancer with integrated positron-emission tomography and computed tomography. *N Engl J Med* **348**, 2500–2507.

[6] Wang D, Schultz CJ, Jursinic PA, Bialkowski M, Zhu XR, Brown WD, Rand SD, Michel MA, Campbell BH, Wong S, et al. (2006). Initial experience of FDG-PET/CT guided IMRT of head-and-neck carcinoma. *Int J Radiat Oncol Biol Phys* **65**, 143–151.

[7] Biehl KJ, Kong FM, Dehdashti F, Jin JY, Mutic S, El Naqa I, Siegel BA, and Bradley JD (2006). 18F-FDG PET definition of gross tumor volume for radiotherapy of non−small cell lung cancer: is a single standardized uptake value threshold approach appropriate? *J Nucl Med* **47**, 1808–1812.

[8] Daisne JF, Duprez T, Weynand B, Lonneux M, Hamoir M, Reychler H, and Grégoire V (2004). Tumor volume in pharyngolaryngeal squamous cell carcinoma: comparison at CT, MR imaging, and FDG PET and validation with surgical specimen. *Radiology* **233**, 93–100.

[9] van Baardwijk A, Baumert BG, Bosmans G, van Kroonenburgh M, Stroobants S, Gregoire V, Lambin P, and De Ruysscher (2006). The current status of FDG-PET in tumour volume definition in radiotherapy treatment planning. *Cancer Treat Rev* **32**, 245–260.

[10] Koukourakis MI, Giatromanolaki A, Harris AL, and Sivridis E (2006). Comparison of metabolic pathways between cancer cells and stromal cells in colorectal carcinomas: a metabolic survival role for tumor-associated stroma. *Cancer Res* **66**, 632–637.

[11] Warburg O (1956). On the origin of cancer cells. *Science* **123**, 309–314.

[12] Robey IF, Lien AD, Welsh SJ, Baggett BK, and Gillies RJ (2005). Hypoxia-inducible factor-1alpha and the glycolytic phenotype in tumors. *Neoplasia* **7**, 324–330.

[13] Pouysségur J, Dayan F, and Mazure NM (2006). Hypoxia signalling in cancer and approaches to enforce tumour regression. *Nature* **441**, 437–443.

[14] Liu D and Hornsby PJ (2007). Fibroblast stimulation of blood vessel development and cancer cell invasion in a subrenal capsule xenograft

model: stress-induced premature senescence does not increase effect. *Neoplasia* **9**, 418–426.

[15] Eskey CJ, Koretsky AP, Domach MM, and Jain RK (1993). Role of oxygen *vs* glucose in energy metabolism in a mammary carcinoma perfused *ex vivo*: direct measurement by ^{31}P NMR. *Proc Natl Acad Sci USA* **90**, 2646–2650.

[16] Tatum JL, Kelloff GJ, Gillies RJ, Arbeit JM, Brown JM, Chao KS, Chapman JD, Eckelman WC, Fyles AW, Giaccia AJ, et al. (2006). Hypoxia: importance in tumor biology, noninvasive measurement by imaging, and value of its measurement in the management of cancer therapy. *Int J Radiat Biol* **82**, 699–757.

[17] Orimo A, Gupta PB, Sgroi DC, Arenzana-Seisdedos F, Delaunay T, Naeem R, Carey VJ, Richardson AL, and Weinberg RA (2005). Stromal fibroblasts present in invasive human breast carcinomas promote tumor growth and angiogenesis through elevated SDF-1/CXCL12 secretion. *Cell* **121**, 335–348.

[18] Zechmann CM, Woenne EC, Brix G, Radzwill N, Ilg M, Bachert P, Peschke P, Kirsch S, Kauczor HU, Delorme S, et al. (2007). Impact of stroma on the growth, microcirculation, and metabolism of experimental prostate tumors. *Neoplasia* **9**, 57–67.

[19] Bhowmick NA, Neilson EG, and Moses HL (2004). Stromal fibroblasts in cancer initiation and progression. *Nature* **432**, 332–337.

[20] Walker RA (2001). The complexities of breast cancer desmoplasia. *Breast Cancer Res* **3**, 143–145.

[21] Beatty JD, Atwood M, Tickman R, and Reiner M (2006). Metaplastic breast cancer: clinical significance. *Am J Surg* **191**, 657–664.

[22] Barnes PJ, Boutilier R, Chiasson D, and Rayson D (2005). Metaplastic breast carcinoma: clinical–pathologic characteristics and HER2/neu expression. *Breast Cancer Res Treat* **91**, 173–178.

[23] Hill R, Song Y, Cardiff RD, and Van Dyke T (2005). Selective evolution of stromal mesenchyme with p53 loss in response to epithelial tumorigenesis. *Cell* **123**, 1001–1011.

[24] Knutson KL, Lu H, Stone B, Reiman JM, Behrens MD, Prosperi CM, Gad EA, Smorlesi A, and Disis ML (2006). Immunoediting of cancers may lead to epithelial to mesenchymal transition. *J Immunol* **177**, 1526–1533.

[25] Moody SE, Perez D, Pan TC, Sarkisian CJ, Portocarrero CP, Sterner CJ, Notorfrancesco KL, Cardiff RD, and Chodosh LA (2005). The transcriptional repressor Snail promotes mammary tumor recurrence. *Cancer Cell* **8**, 197–209.

[26] Knutson KL, Almand B, Dang Y, and Disis ML (2004). Neu antigen–negative variants can be generated after neu-specific antibody therapy in neu transgenic mice. *Cancer Res* **64**, 1146–1151.

[27] Galiè M, Sorrentino C, Montani M, Micossi L, Di Carlo E, D'Antuono T, Calderan L, Marzola P, Benati D, Merigo F, et al. (2005). Mammary carcinoma provides highly tumourigenic and invasive reactive stromal cells. *Carcinogenesis* **26**, 1868–1878.

[28] Ferrier MC, Sarin H, Fung SH, Schatlo B, Pluta RM, Gupta SN, Choyke PL, Oldfield EH, Thomasson D, and Butman JA (2007). Validation of dynamic contrast-enhanced magnetic resonance imaging–derived vascular permeability measurements using quantitative autoradiography in the RG2 rat brain tumor model. *Neoplasia* **9**, 546–555.

[29] Marzola P, Ramponi S, Nicolato E, Lovati E, Sandri M, Calderan L, Crescimanno C, Merigo F, Sbarbati A, Grotti A, et al. (2005). Effect of tamoxifen in an experimental model of breast tumor studied by dynamic contrast-enhanced magnetic resonance imaging and different contrast agents. *Invest Radiol* **40**, 421–429.

[30] Spinelli AE, D'Ambrosio D, Pettinato C, Trespidi S, Nanni C, Ambrosini V, Baldazzi G, Bergamini C, and Marengo M (2006). Performance evaluation of a small animal PET scanner. Spatial resolution characterization using 18-FDG-PET and 11-C. *Nucl Instrum Methods* **571**, 215–218.

[31] Pathak AP, Artemov D, Ward BD, Jackson DG, Neeman M, and Bhujwalla ZM (2005). Characterizing extravascular fluid transport of macromolecules in the tumor interstitium by magnetic resonance imaging. *Cancer Res* **65**, 1425–1432.

[32] Hoekstra CJ, Paglianiti I, Hoekstra OS, Smit EF, Postmus PE, Teule GJ, and Lammertsma AA (2000). Monitoring response to therapy in cancer using [^{18}F]-2-fluoro-2-deoxy-D-glucose and positron emission tomography: an overview of different analytical methods. *Eur J Nucl Med* **27**, 731–743.

[33] Marzola P, Degrassi A, Calderan L, Farace P, Nicolato E, Crescimanno C, Sandri M, Giusti A, Pesenti E, Terron A, et al. (2005). Early antiangiogenic activity of SU11248 evaluated *in vivo* by dynamic contrast-enhanced magnetic resonance imaging in an experimental model of colon carcinoma. *Clin Cancer Res* **11**, 5827–5832.

[34] Marzola P, Farace P, Calderan L, Crescimanno C, Lunati E, Nicolato E, Benati D, Degrassi A, Terron A, Klapwijk J, et al. (2003). *In vivo* mapping of fractional plasma volume (fpv) and endothelial transfer coefficient (Kps) in solid tumors using a macromolecular contrast agent: correlation with histology and ultrastructure. *Int J Cancer* **104**, 462–468.

[35] Hunter GJ, Hamberg LM, Choi N, Jain RK, McCloud T, and Fischman AJ (1998). Dynamic T_1-weighted magnetic resonance imaging and positron emission tomography in patients with lung cancer: correlating vascular physiology with glucose metabolism. *Clin Cancer Res* **4**, 949–955.

[36] van Laarhoven HW, de Geus-Oei LF, Wiering B, Lok J, Rijpkema M, Kaanders JH, Krabbe PF, Ruers T, Punt CJ, van der Kogel AJ, et al. (2005). Gadopentetate dimeglumine and FDG uptake in liver metastases of colorectal carcinoma as determined with MR imaging and PET. *Radiology* **237**, 181–188.

[37] Galie M, D'Onofrio M, Montani M, Amici A, Calderan L, Marzola P, Benati D, Merigo F, Marchini C, and Sbarbati A (2005). Tumor vessel compression hinders perfusion of ultrasonographic contrast agents. *Neoplasia* **7**, 528–536.

[38] Raman V, Artemov D, Pathak AP, Winnard PT Jr, McNutt S, Yudina A, Bogdanov A Jr, and Bhujwalla ZM (2006). Characterizing vascular parameters in hypoxic regions: a combined magnetic resonance and optical imaging study of a human prostate cancer model. *Cancer Res* **66**, 9929–9936.

[39] Airley R, Loncaster J, Davidson S, Bromley M, Roberts S, Patterson A, Hunter R, Stratford I, and West C (2001). Glucose transporter glut-1 expression correlates with tumor hypoxia and predicts metastasis-free survival in advanced carcinoma of the cervix. *Clin Cancer Res* **7**, 928–934.

[40] Zhu Q, Kurtzma SH, Hegde P, Tannenbaum S, Kane M, Huang M, Chen NG, Jagjivan B, and Zarfos K (2005). Utilizing optical tomography with ultrasound localization to image heterogeneous hemoglobin distribution in large breast cancers. *Neoplasia* **7**, 263–270.

[41] Koukourakis MI, Giatromanolaki A, Sivridis E, Gatter KC, and Harris AL (2005). Pyruvate dehydrogenase and pyruvate dehydrogenase kinase expression in non small cell lung cancer and tumor-associated stroma. *Neoplasia* **7**, 1–6.

[42] Gibson GR, Qian D, Ku JK, and Lai LL (2005). Metaplastic breast cancer: clinical features and outcomes. *Am Surg* **71**, 725–730.

[43] Sivridis E, Giatromanolaki A, and Koukourakis MI (2005). Proliferating fibroblasts at the invading tumour edge of colorectal adenocarcinomas are associated with endogenous markers of hypoxia, acidity, and oxidative stress. *J Clin Pathol* **58**, 1033–1038.

[44] Tsarfaty G, Stein GY, Moshitch-Moshkovitz S, Kaufman DW, Cao B, Resau JH, Vande Woude GF, and Tsarfaty I (2006). HGF/SF increases tumor blood volume: a novel tool for the *in vivo* functional molecular imaging of Met. *Neoplasia* **8**, 344–352.

[45] Pennacchietti S, Michieli P, Galluzzo M, Mazzone M, Giordano S, and Comoglio PM (2003). Hypoxia promotes invasive growth by transcriptional activation of the *met* protooncogene. *Cancer Cell* **3**, 347–361.

[46] Anderson GR, Stoler DL, and Scarcello LA (1989). Normal fibroblasts responding to anoxia exhibit features of the malignant phenotype. *J Biol Chem* **264**, 14885–14892.

[47] Gardner LB, Li F, Yang X, and Dang CV (2003). Anoxic fibroblasts activate a replication checkpoint that is bypassed by E1a. *Mol Cell Biol* **23**, 9032–9045.

[48] De Wever O and Mareel M (2003). Role of tissue stroma in cancer cell invasion. *J Pathol* **200**, 429–447.

[49] Bos R, van Der Hoeven JJ, van Der Wall E, van Der Groep P, van Diest PJ, Comans EF, Joshi U, Semenza GL, Hoekstra OS, Lammertsma AA, et al. (2002). Biologic correlates of (18)fluorodeoxyglucose uptake in human breast cancer measured by positron emission tomography. *J Clin Oncol* **20**, 379–387.

[50] Miles KA, Griffiths MR, and Keith CJ (2006). Blood flow–metabolic relationships are dependent on tumour size in non–small cell lung cancer: a study using quantitative contrast-enhanced computer tomography and positron emission tomography. *Eur J Nucl Med Mol Imaging* **33**, 22–28.

[51] Al Sayed AD, El Weshi AN, Tulbah AM, Rahal MM, and Ezzat AA (2006). Metaplastic carcinoma of the breast clinical presentation, treatment results and prognostic factors. *Acta Oncol* **45**, 188–195.

[52] Thiery JP and Sleeman JP (2006). Complex networks orchestrate epithelial–mesenchymal transitions. *Nat Rev Mol Cell Biol* **7**, 131–142.

[53] Frank SJ, Chao KS, Schwartz DL, Weber RS, Apisarnthanarax S, and Macapinlac HA (2005). Technology insight: PET and PET/CT in head and neck tumor staging and radiation therapy planning. *Nat Clin Pract Oncol* **2**, 526–533.